Observing Er³⁺ Sites in Si With an *In Situ* Single-Photon Detector

Ian R. Berkman[1,*] Alexey Lyasota[1] Gabriele G. de Boo[1] John G. Bartholomew[2,3]
Brett C. Johnson[4,5] Jeffrey C. McCallum[4] Bin-Bin Xu[1] Shouyi Xie[1] Rose L. Ahlefeldt[6]
Matthew J. Sellars[6] Chunming Yin[1,7] and Sven Rogge[1]

[1] *Centre of Excellence for Quantum Computation and Communication Technology, School of Physics, University of New South Wales, Sydney, NSW 2052, Australia*

[2] *Centre for Engineered Quantum Systems, School of Physics, The University of Sydney, Sydney, NSW 2006, Australia*

[3] *The University of Sydney Nano Institute, The University of Sydney, Sydney, NSW 2006, Australia*

[4] *Centre of Excellence for Quantum Computation and Communication Technology, School of Physics, University of Melbourne, Victoria 3010, Australia*

[5] *Centre of Excellence for Quantum Computation and Communication Technology, School of Engineering, RMIT University, Victoria 3001, Australia*

[6] *Centre of Excellence for Quantum Computation and Communication Technology, Research School of Physics, Australian National University, Canberra, ACT 0200, Australia*

[7] *CAS Key Laboratory of Microscale Magnetic Resonance and School of Physical Sciences, University of Science and Technology of China, Hefei 230026, China*

We present a flexible method to study the optical properties of an Er³⁺ ensemble in Si accessed via resonant excitation and *in situ* single-photon detection. The technique allows an efficient resonant photoluminescence detection of optically active centers with weak oscillator strength in transparent crystals without the need for nanofabrication on the sample. We observe 70 Er³⁺ resonances in Si, of which 62 resonances have not been observed in the literature, with optical lifetimes ranging from 0.5 to 1.5 ms. We observe inhomogeneous broadening of less than 400 MHz and an upper bound on the homogeneous linewidth of 0.75 and 1.4 MHz for two separate resonances. These narrow, stable resonances confirm Er³⁺ in Si as a promising quantum information candidate. We discuss the use of this technique for rapid characterization of future samples, with the aim of enhancing the prevalence of sites which are favorable for quantum information applications.

I. INTRODUCTION

Rare-earth (RE) ions embedded in a host crystal possess numerous interesting properties for quantum information processing. RE ions can have near-lifetime limited coherence times on their optical transitions [1], as long as 4.4 ms [2], and hyperfine coherence times from seconds to hours in carefully controlled magnetic fields [3,4]. While RE ions have weaker oscillator strengths than other solid-state optical emitters, single-ion detection has been achieved in multiple host crystals, including YAlO₃ [5,6], YVO₄ [7], Y₂SiO₅ [8–10], and Si [11]. These properties make RE ions in solid-state hosts excellent materials for quantum memories [3,12] and potential candidates for qubits [13].

Of particular interest is Er³⁺ because it has a transition between the lowest crystal field levels of the ⁴I₁₅/₂ ground multiplet and the ⁴I₁₃/₂ excited multiplet at approximately 1540 nm, within the technologically useful telecom C band. This convenient wavelength makes Er³⁺ particularly attractive for quantum communication devices and applications. Incorporating Er³⁺ into Si, by means, such as ion implantation or chemical vapor deposition, allows integration into standard complementary metal-oxide-semiconductor processing and provides the ability to fabricate nanophotonic structures [14]. Furthermore, Si can be enriched to nuclear-spin-free ²⁸Si with less than 1 ppm ²⁹Si, resulting in a low magnetic noise environment [15,16], which leads to linewidths as narrow as 33 MHz for T centers [17] and 5 MHz for the donor-bound excitons [18] in Si.

Er³⁺ in Si is known to occupy a wide variety of both substitutional and interstitial sites [19,20]. The nature and

symmetry of many of these sites is, as yet, unknown and a broad parameter space is still to be explored. Characterizing these sites will allow those with ideal properties for quantum information applications to be identified, such as long coherence times, low spectral diffusion, or cyclic optical transitions. Further, knowing the nature of the sites will allow methods to be developed to preferentially create favorable sites. Three main methods are used to characterize these sites: electron paramagnetic resonance (EPR), photoluminescence (PL), and photoluminescence excitation (PLE).

Measurements utilizing EPR probe splittings in the lowest few crystal field levels of the $^4I_{15/2}$ state while PL and PLE probe higher-lying multiplets. In PL, above-band-gap excitation of the Si populates the Er^{3+} excited states via excitation transfer, and fluorescence is monitored from all populated states as the ions decay [20,21]. In PLE, a single optical state of interest is directly excited with a narrow-band laser, and fluorescence is again monitored. Hence, PLE is site selective and particularly suitable for studying the multiple sites in Si. The difficulty of using PLE to study Er^{3+} sites in Si is the low photoluminescence signal due to the ions being distributed over a large number of sites. Nonetheless, PLE of Er^{3+} sites has been observed in Si nanophotonic waveguides [14].

In this paper, we present a flexible and efficient method for the PLE detection of Er^{3+} in Si and characterize their linewidths and lifetimes. The method involves placing a shallow-implanted Er^{3+}:Si chip in direct contact with a superconducting single-photon detector (SSPD), which minimizes coupling losses to the detector and requires no need for nanofabrication of the samples. Samples with different preparation parameters can hence be easily exchanged and characterized, allowing rapid identification of Er^{3+} sites. This is advantageous in the context of optimizing sites for quantum information applications, and allows follow-up measurements, such as probing the spin dynamics or performing spectroscopic scans of single ions. Furthermore, the high efficiency of SSPDs across the spectral range from 250 nm [22] to 7 μm [23–25] indicates that this technique is applicable to other optical sites in Si, such as optical point defects [26,27], and could also be extended to other transparent materials, such as Y_2SiO_5, SiO_2, and $LiNbO_3$.

A. Experiment

In our experiment, implanted Er^{3+} ions in a 1.7×1.7 mm^2 Si chip are resonantly excited with a narrow-band laser and the emission is collected by an *in situ* SSPD. The implanted side is placed against the top of a tungsten-silicide- (WSi) based, optical stack-embedded SSPD. By adjusting the thickness of the optical cavity, the absorption can be tailored to a desired wavelength. We fabricate a SSPD with a minimum system detection efficiency of 50% from 1500 to 1600 nm and with a maximum of 66% at

1550 nm for the measurement [28]. The resulting dark count rate when the laser is turned off is less than 1 kHz.

The chip is sandwiched between the SSPD and an optical fiber that has its core aligned with the SSPD. The latter allows an optical excitation of Er^{3+} ions in direct proximity to the SSPD. Because of the 10 μm mode field diameter of the fiber and the numerical aperture of 0.14, it is expected that the divergence of the optical mode waist through 300-μm Si sample is small, resulting in an optical spot size at the Er^{3+}-rich sample plane comparable to the 15×15 μm^2 working area of the SSPD. Other transparent wafers containing a larger thickness can also be used in this configuration, as the thickness of the sample does not have any effect on the collection efficiency and impacts only the optical spot size at the dopant layer. The reduction in the optical power density in this layer can be counteracted by increasing the laser power. The experiment is operated at 300 mK to ensure a low dark count rate on the SSPD. Moreover, this temperature is low enough to minimize nonradiative recombination of the Er^{3+} [29–31].

To excite the Er^{3+} ions, we use a semiconductor diode laser (Pure Photonics PPCL550) with an output pulse modulated by two acousto-optical modulators (AOMs) connected in series, resulting in an extinction ratio greater than 100 dB [Fig. 1(a)]. After the excitation pulse, we record the number of counts from the SSPD with a digital counter (Keysight 53131A or National Instruments PCI-6602) (see Appendix A for the complete setup).

To study the optical transitions without the complication of hyperfine structure, the nuclear-spin-free ^{170}Er isotope is implanted with multiple ion energies and fluences into one side of the 300-μm double-side-polished Si wafer to form a uniform concentration profile of 1×10^{18} cm^{-3} over a depth of 0.2 μm to 0.6 μm. The wafer contains a background doping of P below 5×10^{15} cm^{-3}. The Er^{3+} concentration is an order of magnitude higher than our single-ion electrical detection experiments [11,32] to provide a strong photoluminescence signal.

The sample is co-implanted with O, as this has been shown to increase Er-related photoluminescence [33,34] and sharp lines in EPR spectroscopy [35]. Hence, O is likewise implanted with multiple energies to create the same depth profile as Er^{3+}, but with a higher concentration of 1×10^{19} cm^{-3}.

Following implantation, the wafer is diced and annealed at 700°C for 10 min in an N_2 atmosphere, which is known to lead to optically active Er^{3+} ions in silicon [11,14]. Afterwards, a 190-nm-thick SiN$_x$ antireflective coating is deposited on both sides using plasma-enhanced chemical vapor deposition. Following numerical calculations, the SiN$_x$ antireflective coating improves the optical detection efficiency by approximately 30% for Si wafers and is therefore not essential.
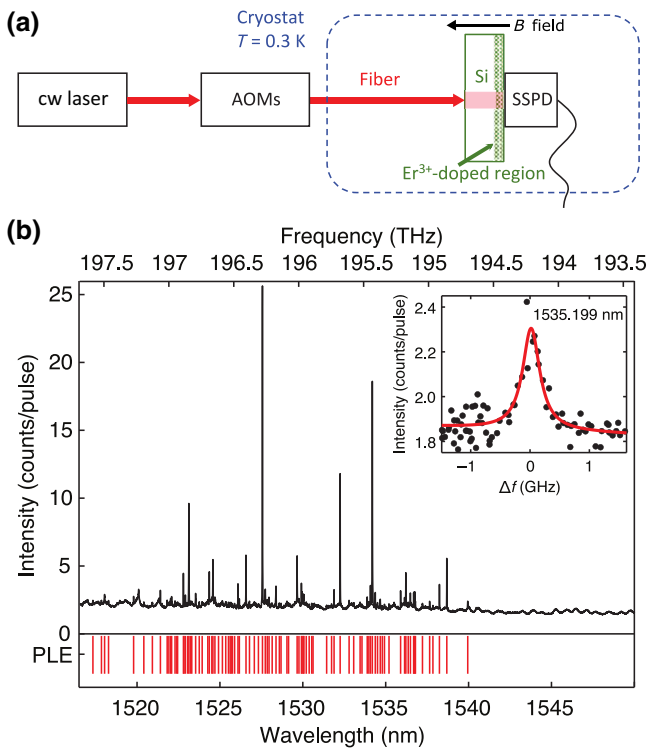
(a)

(b)

FIG. 1. (a) Schematic layout of the experiment (not to scale). The Si sample consisting of a 400-nm Er^{3+}-doped region is placed on top of a SSPD situated in a cryostat at 0.3 K. The PLE spectrum is obtained by producing 100-μs pulses using two acousto-optical modulators with an on:off ratio of more than 100 dB and collecting the luminescence. A magnetic field is applied orthogonal to the sample during the Zeeman measurements. (b) Top: PLE spectrum of Er^{3+}-implanted Si. Bottom: resonance positions for the PLE spectrum (red lines). Inset: a single optically detected inhomogeneous resonance centered at 1535.199 nm, which is fit with a Lorentzian function resulting in a 0.34-GHz full width at half maximum (FWHM) linewidth.

B. Broad spectral survey

A resonant PLE spectrum is obtained by pulsing the laser for 100 μs and integrating the counts from 10 to 900 μs after the pulse [Fig. 1(b)]. This is repeated 1000 times at each optical frequency before the excitation laser is stepped to the next optical frequency. In total, the range of 1516 to 1550 nm is scanned in steps of 50 MHz (0.4 pm). The laser line is broadened with a frequency modulation of 60 MHz in order to avoid stepping over narrow resonances. The laser frequency is monitored at each step with a wavemeter (Bristol 621A).

The SSPD is set to a constant current bias, resulting in a high count rate the first 10 μs after the optical pulse as the SSPD transitioned from a latched resistive state to the superconducting state. The latching is caused by the optical pulse and the additional Joule heating due to the current bias. These high count rates can be prevented by reducing

the current bias to zero during the optical pulse. Furthermore, by pulsing the current bias (see Fig. 7 in Appendix A), the SSPD is able to detect 1.5 μs after the optical pulse. This reset time is consistent with the *RC* time of the SSPD biasing circuit.

The spectrum in Fig. 1(b) consists of 70 peaks, which all displayed a prominence of at least 0.15 counts per pulse and followed a Lorentzian or Gaussian distribution. The resonances with sufficient SNR to distinguish the shape of the distribution, show a better fit to a Lorentzian distribution than a Gaussian distribution. The lower signal-to-noise ratio (SNR) resonances show similar fitting deviations to both distributions. All 70 resonances show an exponential lifetime decay with a milllisecond timescale, consistent with Er^{3+} sites [14,30,31,36,37]. The excitation wavelength, amplitude, Lorentzian FWHM and optical lifetime of the resonances are listed in Appendix I. These resonances consist of different Er^{3+} sites and may include resonances associated with excitation to both the lowest $^4I_{13/2}$ crystal field level, and higher levels. The large number of sites compared to the previous study [14] is explained by the higher Er^{3+} concentration and the formation of more Er−O complexes due to the co-implanted oxygen [19]. The observed resonances have inhomogeneous linewidths ranging from 0.4 to 9.1 GHz, comparable to Er^{3+} in other host crystals [38,39], which can be attributed to different environmental inhomogeneities as well as different sensitivities of the optical transition to these inhomogeneities.

Next, we study the splitting of inhomogeneously broadened resonances under an applied magnetic field to understand their site symmetry. Splitting of an inhomogeneously broadened resonance into a multiple of well-distinguished lines confirms that the Er^{3+} centers reside in well-defined crystallographic sites [40].

In this initial experiment, the magnetic field is applied perpendicular to the SSPD and sample. This field is limited to 60 mT before the SSPD transitioned from a superconducting to a normal state, rendering it unable to detect single photons. Only a few resonances show a resolved splitting below 60 mT. In future experiments, the SSPD could be aligned with the applied field direction. In this arrangement, we find that the SSPD stays superconducting for fields up to 500 mT.

Here, we present the two resonances with the largest splitting under an applied external magnetic field of 50 mT. The first splits into six peaks [Fig. 2(a)] and the second into two peaks with different peak intensities [Fig. 2(b)].

In sites of less than cubic symmetry, Er^{3+} energy levels retain a two-fold Kramers' degeneracy in zero field, which is lifted in an applied magnetic field. This structure gives rise to four different possible optical transitions, assuming the Zeeman splitting in the $^4I_{15/2}$ and $^4I_{13/2}$ differs, as it does in the general case. However, more lines are possible in these ensemble measurements, because if the site
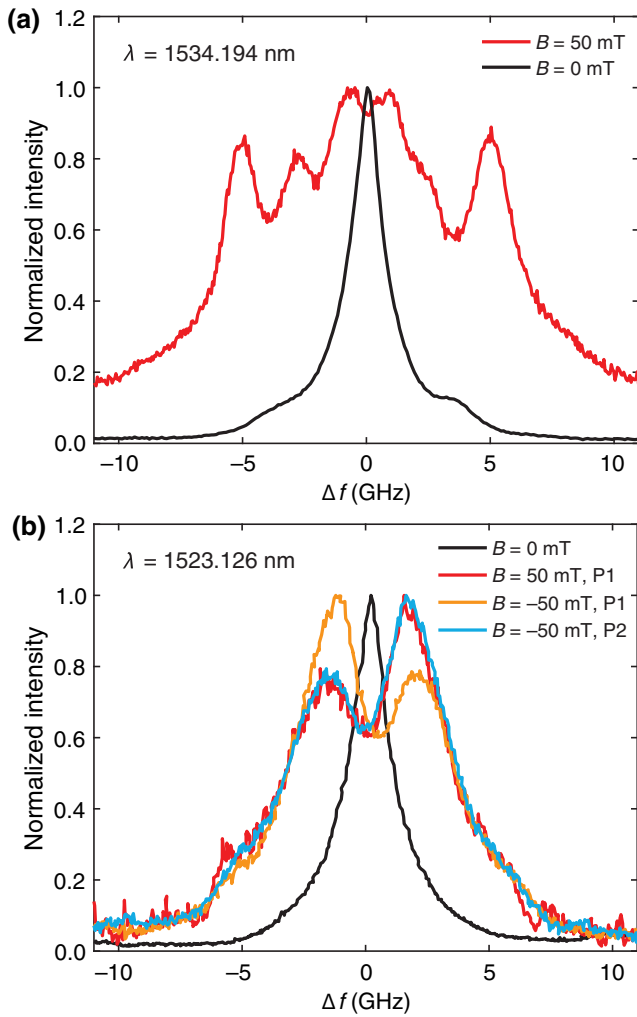
FIG. 2. (a) Inhomogeneously broadened resonance at 1534.194 nm at zero field and the splitting into multiple resonances when 50 mT is applied. (b) Inhomogeneously broadened resonance at 1523.126 nm under −50, 0, and 50 mT. P1 indicates the polarization which results in a maximum intensity of the left peak at −50 mT, while P2 indicates the polarization which results in a maximum intensity of the right peak at −50 mT.

symmetry is lower than the cubic symmetry of the crystal, the site will comprise several magnetically inequivalent subsites with different orientations of the Zeeman tensor (up to 24 in C_1 symmetry). Multiple lines may also be observed if the defect occupies the T_d site in Si without reducing the symmetry, however, in Si, the symmetry will typically be lowered. The splitting into six peaks relating to the transition energies in Fig. 2(a) therefore likely indicates at least two magnetically inequivalent subsites at a lower site symmetry than cubic. The splitting into less than four peaks, as seen in Fig. 2(b), is explained by an underlying unresolved structure, indicated by the broader Zeeman arms compared to the resonance at zero field.

The different peak intensities in Fig. 2(b) can be attributed to different polarization-dependent oscillator strengths, rather than different Boltzmann populations of the initial states, because the relative intensities of the two peaks can be reversed by rotating the polarization using a $\lambda/2$ wave plate. Reversing the magnetic field also reverses the peak intensities, further confirming that the difference is not due to differing Boltzmann populations.

C. Homogeneous broadening

The homogeneous linewidth is investigated in detail using transient spectral hole burning [41] for two resonances with narrow spectral hole properties. The method relies on the nonlinear increase of the fluorescence signal due to saturation of the atomic transition. The laser frequency is modulated using an electro-optical modulator (EOM), creating two sidebands 5 GHz apart while suppressing the carrier (see Appendix B for the setup). The high-frequency sideband at 2.5 GHz from the carrier frequency is centered on the inhomogeneous peak and excited the ensemble for 20 μs, referred to the pump pulse. The low-frequency sideband at −2.5 GHz from the carrier frequency excited an off-resonance region to ensure no additional lines are excited. Immediately after the on-resonance pump pulse, a 20-μs excitation pulse is applied at a slightly detuned laser frequency (2.5 GHz + Δf), referred to as the probe pulse. For an equal pump and probe time, the occupation number of the excited state at the end of both pulses is given by

$$\rho_{ee}(2t_p) = \begin{cases} \rho_{\mathrm{res}}(2t_p) & \text{for } \Delta f = 0 \\ 2\rho_{\mathrm{res}}(t_p)(1 - \frac{1}{2}e^{-t_p/\tau}) & \text{for } \Delta f \gg \gamma_D \end{cases}, \quad (1)$$

where t_p is the pump time, $\rho_{\mathrm{res}}(t)$ is the occupation number when excited on resonance, τ the optical lifetime, and γ_D the homogeneous linewidth [Fig. 3(a)]. The excitation and probe pulse length are chosen to be sufficiently short compared to the optical lifetime that $\rho_{ee}(2t_{\mathrm{pump}}) \approx 2\rho_{\mathrm{res}}(t_{\mathrm{pump}}) > \rho_{\mathrm{res}}(2t_{\mathrm{pump}})$ whenever $\Delta f \gg \gamma_D$. The repetition time of 3 ms is chosen to be twice the optical lifetime, ensuring the majority of excited Er^{3+} ions have decayed into the ground state. To ensure that the off-resonant low-frequency sideband did not affect the spectral hole width, the homogenenous broadening is remeasured while the carrier is present, yielding a comparable width and confirming that the hole width is unaffected by the off-resonant light.

At 1 μW of excitation power on the sample, only the resonances at 1538.685 and 1532.254 nm show narrow spectral holes with sufficient SNR. These spectral holes are studied in detail under 360 nW of excitation power to extract the minimum hole width obtainable in our current setup. The data is fitted with a Lorentzian distribution with a FWHM of 1.5 MHz [Fig. 3(b)] for 1538.685 nm
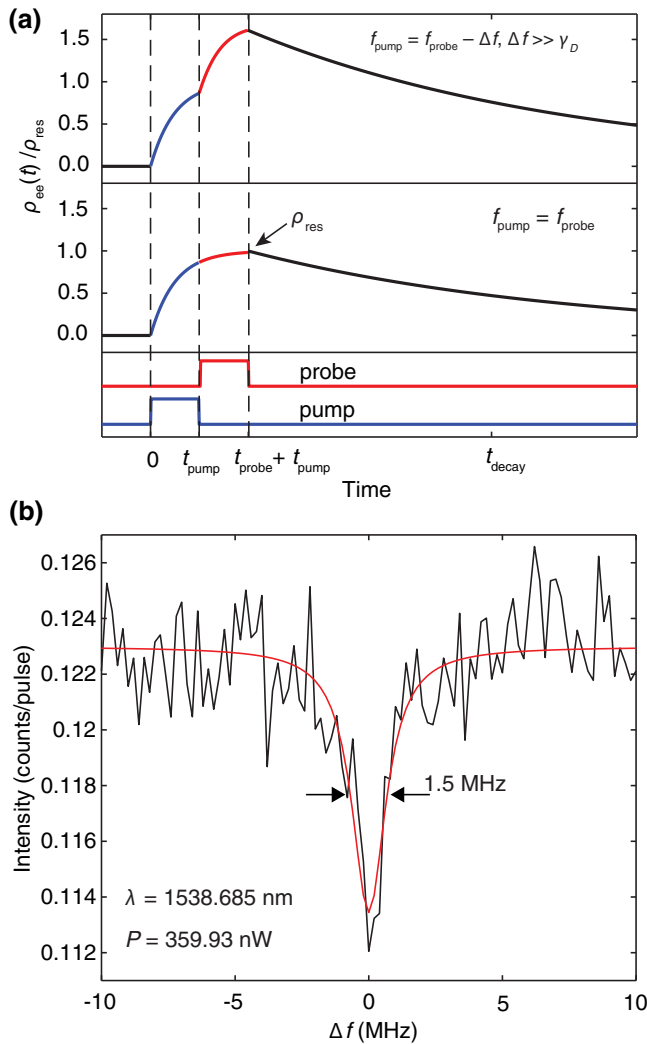
(a) Top: expected decay signal when the probe offset is larger than the homogeneous linewidth. Middle: expected decay signal when the pump and probe frequency are equal. Bottom: pulse sequence for spectral hole measurements. The curves are normalized to $\rho_{res}(t_{pump} + t_{probe})$, which is the occupation number when the subset is resonantly excited. (b) Upper bound on the homogeneous linewidth at 1538.685 nm. The vertical axis gives the integrated number of counts up to 1 ms after the probe pulse as a function of $f_{probe} - f_{pump}$. The data is fitted with a Lorentzian distribution, resulting in a FWHM of 1.5 MHz.

and 2.8 MHz at 1532.254 nm. The upper bound on the homogeneous linewidth is given by half of the spectral hole linewidth [42], leading to a maximum homogeneous linewidth of 0.75 MHz (3.1 neV) and 1.4 MHz (5.8 neV) for 1538.685 and 1532.254 nm, respectively.

To study the timescale of processes resulting in the spectral hole broadening, the hole linewidth is compared for 10 µs pump and probe pulses separated by 0 µs and by 90 µs (see Appendix C for the measurement). The choice of delay is limited by the optical lifetime of the resonance, as a longer delay results in a loss of spectral hole visibility.

A delay of 90 µs did not affect the hole, hence instantaneous spectral diffusion did not play a significant role in the spectral hole linewidth on this timescale.

D. Lifetime

Next, the optical lifetimes of all 70 resonances were measured. The lifetime of Er^{3+} varies according to the radiative lifetime of the transition as well as the background doping of Si [31]. In addition, in this type of fluorescence measurement, the lifetime measured is typically that of the lowest $^4I_{13/2}$ level, regardless of which crystal field level is excited, because higher crystal field levels rapidly decay nonradiatively to the lowest state [43]. In principle, this means that resonances associated with the same site should have identical fluorescence lifetimes.

To measure the fluorescence lifetime, the number of single-photon events is recorded for 5 ms after a 100-µs excitation pulse is centered on the inhomogeneous peak. The signal decay after the excitation pulse did not follow a single exponential curve, but instead is a combination of the resonant signal and a background signal. To separate this background decay, it is measured at an optical frequency where the photoluminescence resonance is absent. It is found to be wavelength independent and consisted of a fast (approximately 200 µs) and a slow (approximately 800 µs) exponential decay [I_{offres} in Fig. 4(a)]. This biexponential decay has been observed previously in Er^{3+}:Si using both photoluminescence [36,37,44,45] and electroluminescence [29]. These fast and slow components are related to the radiative decay of excitons and indirectly excited Er^{3+} ions, respectively. The background is thus attributed to a noncompetitive process and can be subtracted from the resonance decay signal.

To more accurately determine the Er^{3+} lifetime, a nearby background decay is measured at every resonance approximately 2 times the FWHM away [46]. The subtracted signal followed a single exponential decay for most of the resonances, where the largest amplitude decay trace is shown in Fig. 4(a). A number of resonances show a biexponential decay in the subtracted signal, marked by b in Table I and several biexponential traces can be found in Ref. [46].

A summary of the lifetimes is presented in Table I. The optical lifetimes range from 0.5 to 1.5 ms, similar to lifetimes found in various PL and PLE experiments [14,30,31,36,37] as well as what is expected on theoretical grounds for magnetic dipole transitions [47]. No other defects in Si contain a lifetime over 0.5 ms except for S [48]. Since the contamination levels of S in the Si wafer and introduced during ion implantation are negligible, the 70 resonances are associated with Er^{3+} sites. Compared to the PLE results in Ref. [14], for the seven resonances that are found in both experiments we find a
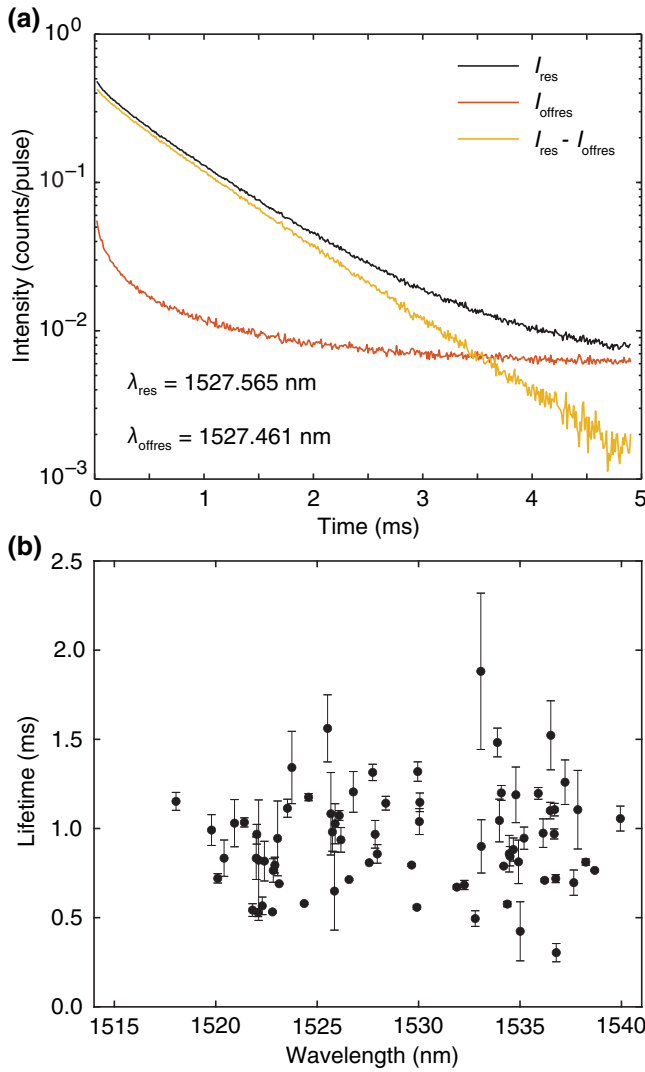
(a)

(b)

FIG. 4. (a) Photoluminescence decay curve for the resonance at 1527.565 nm (I_{res}) and the background at 1527.461 nm (I_{offres}). The on-resonant time trace shows a biexponential decay, which is due to the biexponential off-resonant decay. Since the off-resonant decay is due to noncompetitive processes, the Er^{3+} decay can be extracted by subtracting the off-resonant time trace, resulting in a single exponential decay except for a few, as can be found in Table I. (b) Fit result of the lifetime for the 70 resonances. Errorbars show the standard error of the fit.

shorter lifetime for each resonance, with the average difference being 250 µs. The two experiments use different samples, excitation methods and detection geometries, and two mechanisms could explain the different numbers: extra nonradiative decay in our system, or fluorescence trapping in the measurements of Ref. [14].

A large number of lines are obtained with lifetimes all close to 1 ms [Fig. 4(b)]. The small variations in lifetime can be explained by the different sites and emission from different crystal field levels.

II. DISCUSSION

The results described above show that this *in situ* detection method results in a sufficient collection efficiency to observe a very large number of sites. Furthermore, this technique detects optically active sites over 5 orders of magnitude dynamic range, with a lower bound at 170 Hz, corresponding to 1525.848 nm in Table I and an upper bound of 25 MHz, limited by internal kinetic inductance of the SSPD [49]. As the SSPD has a dark count rate of less than 1 kHz, it is expected that count rates down to 10 Hz on the detectors can be observed, which should allow the study of single ions.

Given the ease of studying multiple samples with this method, various sample parameters can be investigated and optimized with the aim of increasing the prevalence of sites with the narrow homogeneous and inhomogeneous linewidths desired for quantum information applications. Future samples of interest include lower Er and O concentrations, different annealing procedures and the use of nuclear-spin-free ^{28}Si as host crystal.

The narrow inhomogeneous linewidth and submegahertz optical homogeneous linewidth presented in this paper at a high Er^{3+} and O concentration show that Er^{3+} ions in Si is a promising platform for quantum photonics applications, such as Er^{3+}-based single-photon sources [50]. The practical applications of Er^{3+}-based single-photon sources for optical quantum computing rely on the ability to compensate for the relatively weak Er^{3+} oscillator strength by integrating Er^{3+} ions with photonic cavities [7–9,38,51].

The emission rate of Er^{3+} ions in photonic cavities is given by $\gamma_{cav} = \beta F \gamma_{bulk}$ assuming $\gamma_{cav} \gg \gamma_{bulk}$, where F, γ_{bulk}, and $\beta = 0.2$ are the Purcell factor, the Er^{3+} emission rate and the branching ratio for Er^{3+} in bulk Si into the optical transition resonant with the cavity mode, respectively. The maximum Purcell factor is achieved when the system operates at the transition between the weak and strong coupling regimes [52]. At this transition, the cavity mode energy damping rate is $\kappa = 4g$ and $\gamma_{cav} = 2g$, where g is the optical transition-cavity mode coupling strength. Then, the maximum Purcell factor given by $F = 2g/(\beta \gamma_{bulk})$ is defined by the cavity design and the corresponding cavity mode volume $V_m = 3\lambda^2 c/(2\pi n^3 F^2 \beta \gamma_{bulk})$ ($V_m = 3\lambda^2 c \beta \gamma_{bulk}/(8\pi n^3 g^2)$). Here, κ and g are in angular frequency units.

A Purcell factor of approximately 2×10^6, corresponding to an Er^{3+} emission rate of 400 MHz, would approach the state-of-the-art single-photon source brightness [14]. To achieve this regime requires an upper bound on the cavity mode volume of $V_m = 0.1(\lambda/n)^3$ ($g = 2\pi \times 30$ MHz) for the Er^{3+} spontaneous emission rate in Si ($\gamma_{bulk} = 1$ kHz). Such a cavity mode volume can be achieved in nanobeam Si photonic cavities [53,54]. The corresponding quality factor $Q = 1.5 \times 10^6$ ($\kappa = 120$ MHz) is close to

the state-of-the-art values in nanobeam cavities [55] but still has to be practically realized. To achieve a Purcell enhancement of 6 orders of magnitude in lower-quality factor cavities would require ultralow mode volumes, such as those available in bowtie photonic crystal cavities [56]. If these extremely high Purcell factors can be realized, the Er^{3+} homogeneous linewidth could be engineered to be limited by radiative broadening that exceeds the other broadening rates by 3 orders of magnitude. This would make Er^{3+} in Si a promising platform for creating single-photon sources with high brightness and single-photon indistinguishability.

III. CONCLUSION

In this paper we use an *in situ* PLE method to study, in detail, the inhomogeneous linewidths and lifetimes of 70 Er^{3+} resonances in Si, only eight of which have previously been observed [14,57]. The homogeneous linewidths of two bright resonances are found to be 0.75 and 1.4 MHz, indicating sub-MHz linewidths of multiple sites can be expected with sample optimization. The narrow linewidths presented show that Er^{3+} in Si is a promising system for quantum information and communication purposes, and further refinement is achievable using the current approach due to the rapid preparation of samples so a broad parameter space can be explored efficiently.

APPENDIX A: PHOTOLUMINESCENT EXCITATION SPECTRUM SETUP

A schematic of the setup is shown in Fig. 5 and the *in situ* sample and optical stack-embedded SSPD in Fig. 6. The continuous-wave laser was a Pure Photonics PPCL550, which is attenuated to reach low optical power levels. Afterwards, the light is split using a 90:10 beam splitter where the low output port is connected to a Bristol 621A wavelength meter. Following the beam splitter are two AOMs, which are pulsed using an arbitrary waveform generator. A 90:10 beam splitter is used to direct 10% of the light to an optical power meter. The higher output end
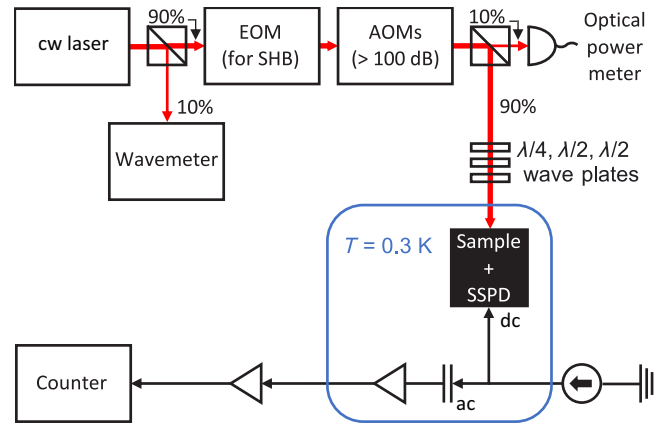

FIG. 5. Experimental setup. A continuous-wave laser provided narrow-band light. A portion of the laser light is monitored by the wavemeter. The EOM is added when performing the spectral hole burning measurements. Two AOMs are used to pulse the intensity of the light with a contrast of over 100 dB. Ten percent of the laser light continued to an optical power meter to calculate the power on the sample. The other portion of the laser light continued through polarization paddles to control the polarization on the sample. The sample, SSPD, bias tee, and HEMT amplifier are inside the HelioxVL at 300 mK. The high-frequency SSPD signal coupled out through the HEMT amplifier and two room-temperature amplifiers into the counter.

is directed to polarization paddles to adjust the polarization for the magnetic field measurements. A schematic is shown in Fig. 5.

The fiber is coupled into an Oxford HelioxVL, which resides in an Oxford magnet dewar. The HelioxVL contains the sample, SSPD, bias-tee, and a homemade high-electron-mobility transistor (HEMT) amplifier. A bias current is applied to the SSPD, and the 2-ns pulse is read out via a bias tee. The ac SSPD signal is amplified at room temperature using two rf amplifiers. The pulse is stretched using a homemade double-comparator pulse stretcher and read out using a National Instruments 6602 counter card. The counter card is initialized to measure the number of counts in 10 μs bins.

For the PLE spectrum in the main text [Fig. 1(b)] the SSPD current is kept constant at the switching current I_{sw} where the detection efficiency is maximum [49]. The count rates in the first 10 μs after the end of the optical pulse are ignored, since these count rates are significantly higher than the count rates originating from the Er^{3+} due to the SSPD transition from a latched resistive state to a superconducting state.

Alternatively, the SSPD current can be biased, where the current reduces to zero during the optical pulse (see Fig. 7) to decrease the resistive-to-superconducting-state induced high count rate and to reduce the reset time of the SSPD after the optical pulse. In this approach, the SSPD reached the nominal detection efficiency value 1.5 μs after the end
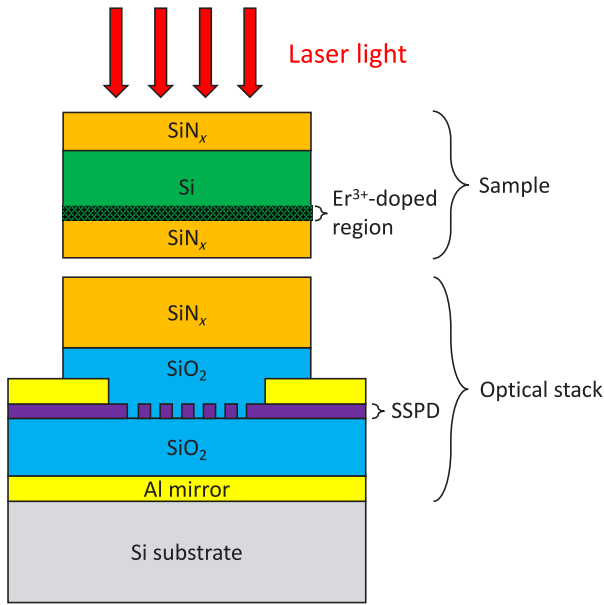
FIG. 6. Direction of the laser light, the sample, and optical stack-embedded SSPD (not to scale). The sample is coated with 190 nm of SiN_x on both sides to enhance the transmission through the sample. The chip is placed upside down on the SSPD stack so the 400 nm Er^{3+}-doped region is in close proximity with the SSPD. The SSPD is embedded in an optical stack to increase the collection efficiency. A fiber is placed on top of the sample, which provides the laser light and clamps the sample on top of the SSPD. The remaining air gap between the sample and the SSPD is limited by the flatness of both surfaces.

of the optical pulse, which is consistent with the *RC* time of the SSPD biasing circuit.

APPENDIX B: SPECTRAL HOLE BURNING SETUP

To perform the spectral hole burning measurements, an EOM is connected in series before the AOMs. A voltage source is connected to the dc port and two rf sources are combined using a rf combiner and connected to the rf port of the EOM. Both rf sources are pulse triggered by the leading edge of the AOMs signal. The first rf source is set to 2.5 GHz and 0 dBm and the second rf source is set to $\Delta f + 2.5$ GHz, where Δf is the detuning frequency. The power of the second rf source is normalized to result in the same optical power as the first rf source at different rf frequencies. To pulse both rf sources externally, the sync output of the arbitrary waveform generator used to pulse the AOMs is connected to the pulse modulation input of both rf sources. To align the pulses, delays are implemented in the system, which are calibrated by monitoring the light intensity on a 125 MHz (In, Ga)As photodiode, connected to an oscilloscope.

The EOM is initialized by turning the rf sources off and the laser on and adjusting the dc voltage until it showed a maximum extinction of the carrier. Additionally, the
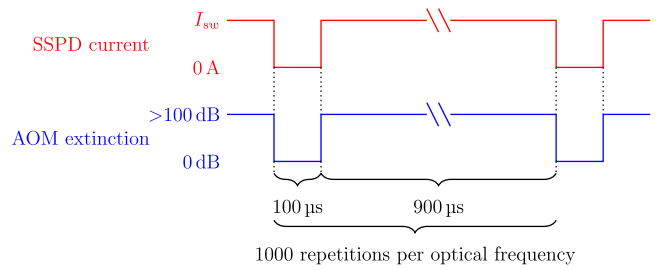

FIG. 7. Pulsing schematic for the pulsed bias current measurements. During the 100-μs long optical pulse, the superconducting single-photon detector (SSPD) current is reduced from the switching current (I_{sw}) to 0 A. Afterwards, the bias current is increased to I_{sw} for 900 μs so the SSPD is able to detect the single photons for 900 μs after the end of the optical pulse. This pulse sequence is repeated 1000 times at a fixed optical frequency before the laser frequency is changed to the next frequency. The minimum time required for the SSPD to detect the single photons after the end of the optical pulse is 1.5 μs. This reset time corresponded to the *RC* time of the SSPD biasing circuit.

polarization is adjusted to extinguish the carrier further. The rf signal is turned on to create the sidebands, and the polarization fine tuned until the ratio of the optical power when the rf source is on and off is maximized. The extinction of the carrier when the rf source is on, is confirmed by sweeping both sidebands over an inhomogeneous peak. The extinction ratio is over 15 dB in our spectral hole burning measurements.

APPENDIX C: SPECTRAL DIFFUSION

To inspect the time scale of diffusion processes, the spectral hole burning is performed with a 0-μs and 90-μs delay between the two pulses. The result is presented in
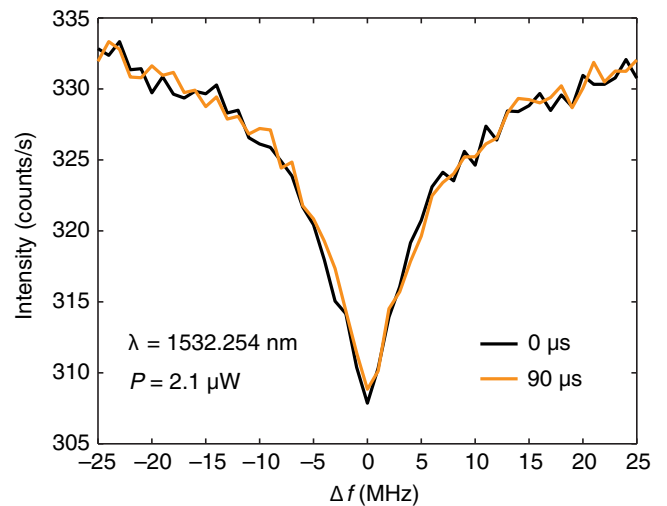

FIG. 8. Overlapping plots of spectral hole burning with two different delays at 0 μs and 90 μs. The linewidth of the two holes are approximately equal regardless of the delay between the pulses.

Fig. 8 for a pump and probe pulse of 10 μs each. The pump and probe pulse are shortened compared to the measurement in Fig. 3 in the main text to ensure the duration of the pulses is short compared to the 90-μs delay. The linewidth of the two spectral holes are equal and it can therefore be concluded that spectral diffusion is caused by fast diffusion processes during optical excitation, pointing towards instantaneous spectral diffusion as a dominant spectral hole broadening mechanism.

APPENDIX D: DETECTED Er^{3+} RESONANCES

We observe 70 Er^{3+} resonances in the PLE spectrum. Of these resonances, the center wavelength, inhomogeneous linewidth, lifetime and amplitude are collected and summarized in Table I.

TABLE I. Overview table of the measured wavelength in vacuum, the Lorentzian FWHM of the inhomogeneous broadening, the optical lifetime, and the peak amplitude corresponding to the integrated number of counts from 10 μs to 900 μs after the pulse.

Wavelength (nm)	Linewidth (GHz)	Lifetime (ms)	Amplitude (counts/pulse)
1539.949	2.82	1.05	0.59
1538.685[a]	1.02	0.764	4.06
1538.242	1.81	0.810	1.73
1537.851	3.5	1.1	0.26
1537.652	1.95	0.70	0.57
1537.220	2.5	1.26	0.31
1536.762	0.40	0.72	1.29
1536.708	0.94	1.11	0.84
1536.687	1.5	0.97	1.13
1536.518	0.5	1.52	0.25
1536.489	1.30	1.10	0.95
1536.215[ba]	1.64	0.708	2.39
1536.137	1.7	0.97	0.61
1535.899	0.83	1.19	1.40
1535.199	0.34	0.94	0.45
1534.924	4.8	0.81	0.25
1534.796	0.42	1.19	0.27
1534.672	4.7	0.88	0.57
1534.506	1.3	0.84	0.36
1534.469	3.2	0.86	0.31
1534.371[a]	2.17	0.575	1.00
1534.195[ba]	1.76	0.788	15.96
1534.080	1.26	1.20	1.41
1533.985	2.3	1.04	0.30
1533.885	2.08	1.48	0.80
1533.087	3.2	0.90	0.30
1532.792[a]	1.6	0.49	0.41
1532.254[ba]	1.208	0.682	10.63
1531.886	0.47	0.670	1.83
1530.062	1.69	1.15	0.77
1530.034	4.5	1.04	0.78
1529.955	3.5	1.32	0.95
1529.916[ba]	0.97	0.557	1.61

Continued.

TABLE I. Continued.

Wavelength (nm)	Linewidth (GHz)	Lifetime (ms)	Amplitude (counts/pulse)
1529.657	1.68	0.793	3.31
1528.380	3.9	1.14	1.53
1527.963	3.9	0.86	0.69
1527.851	6.9	0.97	0.41
1527.735	3.11	1.31	1.06
1527.565	1.43	0.807	25.0
1526.776	4.9	1.20	0.52
1526.572[b]	1.70	0.712	3.84
1526.171	1.74	0.93	0.69
1526.088	1.86	1.07	1.75
1525.885	1.8	1.03	0.24
1525.848	3.5	0.6	0.15
1525.751	2.9	0.98	0.29
1525.677	1.4	1.1	0.28
1525.513	2.8	1.56	0.32
1524.577	2.32	1.17	3.18
1524.360[b]	1.09	0.578	2.41
1523.753	3.2	1.3	0.39
1523.535	3.8	1.11	0.85
1523.126[b]	2.07	0.689	7.45
1523.050	2.9	0.9	0.27
1522.917	2.6	0.79	0.81
1522.835	1.1	0.76	0.49
1522.797[b]	0.74	0.531	2.61
1522.399	1.0	0.82	0.24
1522.291[a]	3.6	0.57	0.39
1522.114	1.0	0.8	0.19
1522.085	1.18	0.53	0.63
1522.025	1.13	0.97	0.48
1521.994	1.2	0.83	0.26
1521.816	2.7	0.54	0.45
1521.409	0.65	1.03	1.25
1520.926	3.6	1.03	0.24
1520.412	2.5	0.83	0.35
1520.094	9.1	0.72	0.86
1519.793	2.2	0.99	0.56
1518.042	5.3	1.15	0.61

[a]Observed in Ref. [14] or [57].
[b]Biexponential decay.

[1] C. W. Thiel, T. Böttger, and R. L. Cone, Rare-earth-doped materials for applications in quantum information storage and signal processing, J. Lumin. **131**, 353 (2011).

[2] T. Böttger, C. W. Thiel, R. L. Cone, and Y. Sun, Effects of magnetic field orientation on optical decoherence in Er^{3+} in Y$_2$SiO$_5$, Phys. Rev. B **79**, 115104 (2009).

[3] M. J. Zhong, M. P. Hedges, R. L. Ahlefeldt, J. G. Bartholomew, S. E. Beavan, S. M. Wittig, J. J. Longdell, and M. J. Sellars, Optically addressable nuclear spins in a solid with a six-hour coherence time, Nature **517**, 177 (2015).

[4] M. Rančić, M. P. Hedges, R. L. Ahlefeldt, and M. J. Sellars, Coherence time of over a second in a telecom-compatible quantum memory storage material, Nat. Phys. **14,** 50 (2017).

[5] R. Kolesov, K. Xia, R. Reuter, R. Stohr, A. Zappe, J. Meijer, P. R. Hemmer, and J. Wrachtrup, Optical detection of a single rare-earth ion in a crystal, Nat. Commun. **3,** 1029 (2012).

[6] P. Siyushev, K. Xia, R. Reuter, M. Jamali, N. Zhao, N. Yang, C. Duan, N. Kukharchyk, A. D. Wieck, R. Kolesov, and J. Wrachtrup, Coherent properties of single rare-earth spin qubits, Nat. Commun. **5,** 3895 (2014).

[7] J. M. Kindem, A. Ruskuc, J. G. Bartholomew, J. Rochman, Y. Q. Huan, and A. Faraon, Control and single-shot readout of an ion embedded in a nanophotonic cavity, Nature **580,** 201 (2020).

[8] M. Raha, S. Chen, C. M. Phenicie, S. Ourari, A. M. Dibos, and J. D. Thompson, Optical quantum nondemolition measurement of a single rare earth ion qubit, Nat. Commun. **11,** 1605 (2020).

[9] S. Chen, M. Raha, C. M. Phenicie, S. Ourari, and J. D. Thompson, Parallel single-shot measurement and coherent control of solid-state spins below the diffraction limit, Science **370,** 592 (2020).

[10] T. Utikal, E. Eichhammer, L. Petersen, A. Renn, S. Goetzinger, and V. Sandoghdar, Spectroscopic detection and state preparation of a single praseodymium ion in a crystal, Nat. Commun. **5,** 3627 (2014).

[11] C. Yin, M. Rančić, G. G. de Boo, N. Stavrias, J. C. McCallum, M. J. Sellars, and S. Rogge, Optical addressing of an individual erbium ion in silicon, Nature **497,** 91 (2013).

[12] T. Zhong, J. M. Kindem, J. G. Bartholomew, J. Rochman, I. Craiciu, E. Miyazono, M. Bettinelli, E. Cavalli, V. Verma, S. W. Nam, F. Marsili, M. D. Shaw, A. D. Beyer, and A. Faraon, Nanophotonic rare-earth quantum memory with optically controlled retrieval, Science **357,** 1392 (2017).

[13] M. Grimm, A. Beckert, G. Aeppli, and M. Müller, Universal quantum computing using electronuclear wavefunctions of rare-earth ions, PRX Quantum **2,** 010312 (2021).

[14] L. Weiss, A. Gritsch, B. Merkel, and A. Reiserer, Erbium dopants in nanophotonic silicon waveguides, Optica **8,** 40 (2021).

[15] M. Steger, K. Saeedi, M. L. W. Thewalt, J. J. L. Morton, H. Riemann, N. V. Abrosimov, P. Becker, and H. J. Pohl, Quantum information storage for over 180 s using donor spins in a Si-28 semiconductor vacuum, Science **336,** 1280 (2012).

[16] J. T. Muhonen, J. P. Dehollain, A. Laucht, F. E. Hudson, R. Kalra, T. Sekiguchi, K. M. Itoh, D. N. Jamieson, J. C. McCallum, A. S. Dzurak, and A. Morello, Storing quantum information for 30 seconds in a nanoelectronic device, Nat. Nanotechnol. **9,** 986 (2014).

[17] L. Bergeron, C. Chartrand, A. T. K. Kurkjian, K. J. Morse, H. Riemann, N. V. Abrosimov, P. Becker, H. J. Pohl, M. L. W. Thewalt, and S. Simmons, Silicon-Integrated Telecommunications Photon-Spin Interface, Phys. Rev. X Quantum **1,** 020301 (2020).

[18] A. Yang, M. Steger, T. Sekiguchi, M. L. W. Thewalt, J. W. Ager, and E. E. Haller, Homogeneous linewidth of the P-31 bound exciton transition in silicon, Appl. Phys. Lett. **95,** 122113 (2009).

[19] A. J. Kenyon, Erbium in silicon, Semicond. Sci. Technol. **20,** R65 (2005).

[20] H. Przybylińska, W. Jantsch, Y. Suprun-Belevitch, M. Stepikhova, L. Palmetshofer, G. Hendorfer, A. Kozanecki, R. J. Wilson, and B. J. Sealy, Optically active erbium centers in silicon, Phys. Rev. B **54,** 2532 (1996).

[21] R. A. Hogg, K. Takahei, and A. Taguchi, Photoluminescence excitation spectroscopy of GaAs:Er, O in the near-band-edge region, J. Appl. Phys. **79,** 8682 (1996).

[22] E. E. Wollman, V. B. Verma, A. D. Beyer, R. M. Briggs, B. Korzh, J. P. Allmaras, F. Marsili, A. E. Lita, R. P. Mirin, S. W. Nam, and M. D. Shaw, UV superconducting nanowire single-photon detectors with high efficiency, low noise, and 4 K operating temperature, Opt. Express **25,** 26792 (2017).

[23] G. Gol'tsman, O. Minaeva, A. Korneev, M. Tarkhov, I. Rubtsova, A. Divochiy, I. Milostnaya, G. Chulkova, N. Kaurova, B. Voronov, D. Pan, J. Kitaygorsky, A. Cross, A. Pearlman, I. Komissarov, W. Slysz, M. Wegrzecki, P. Grabiec, and R. Sobolewski, Middle-infrared to visible-light ultrafast superconducting single-photon detectors, IEEE Trans. Appl. Supercond. **17,** 246 (2007).

[24] F. Marsili, F. Bellei, F. Najafi, A. E. Dane, E. A. Dauler, R. J. Molnar, and K. K. Berggren, Efficient single photon detection from 500 nm to 5 µm wavelength, Nano Lett. **12,** 4799 (2012).

[25] L. Chen, D. Schwarzer, V. B. Verma, M. J. Stevens, F. Marsili, R. P. Mirin, S. W. Nam, and A. M. Wodtke, Mid-infrared laser-induced fluorescence with nanosecond time resolution using a superconducting nanowire single-photon detector: New technology for molecular science, Acc. Chem. Res. **50,** 1400 (2017).

[26] W. Redjem, A. Durand, T. Herzig, A. Benali, S. Pezzagna, J. Meijer, A. Y. Kuznetsov, H. S. Nguyen, S. Cueff, J. M. Gerard, I. Robert-Philip, B. Gil, D. Caliste, P. Pochet, M. Abbarchi, V. Jacques, A. Dreau, and G. Cassabois, Single artificial atoms in silicon emitting at telecom wavelengths, Nat. Electron. **3,** 738 (2020).

[27] D. B. Higginbottom *et al.*, Optical observation of single spins in silicon, Nature **607,** 266 (2022).

[28] See Supplemental Material at http://link.aps.org/supplemental/10.1103/PhysRevApplied.19.014037 for the calculation of the detection efficiency (S-A).

[29] J. Palm, F. Gan, B. Zheng, J. Michel, and L. C. Kimerling, Electroluminescence of erbium-doped silicon, Phys. Rev. B **54,** 17603 (1996).

[30] A. Taguchi, K. Takahei, M. Matsuoka, and S. Tohno, Evaluation of the energy-transfer rate between an Er 4f shell and a Si host in Er-doped Si, J. Appl. Phys. **84,** 4471 (1998).

[31] F. Priolo, G. Franzo, S. Coffa, and A. Carnera, Excitation and nonradiative deexcitation processes of Er^{3+} in crystalline Si, Phys. Rev. B **57,** 4443 (1998).

[32] G. G. de Boo, C. Yin, M. Rančić, B. C. Johnson, J. C. McCallum, M. J. Sellars, and S. Rogge, High-resolution spectroscopy of individual erbium ions in strong magnetic fields, Phys. Rev. B **102,** 155309 (2020).

[33] J. L. Benton, J. Michel, L. C. Kimerling, D. C. Jacobson, Y. H. Xie, D. J. Eaglesham, E. A. Fitzgerald, and J.

M. Poate, The electrical and defect properties of erbium-implanted silicon, J. Appl. Phys. **70,** 2667 (1991).

[34] S. Coffa, F. Priolo, G. Franzo, V. Bellani, A. Carnera, and C. Spinella, Optical activation and excitation mechanisms of Er implanted in Si, Phys. Rev. B **48,** 11782 (1993).

[35] J. D. Carey, J. F. Donegan, R. C. Barklie, F. Priolo, G. Franzo, and S. Coffa, Electron paramagnetic resonance of erbium doped silicon, Appl. Phys. Lett. **69,** 3854 (1996).

[36] S. Coffa, G. Franzo, F. Priolo, A. Polman, and R. Serna, Temperature-dependence and quenching processes of the intra-4f luminescence of Er in crystalline Si, Phys. Rev. B **49,** 16313 (1994).

[37] X. Wu, R. White, U. Hommerich, F. Namavar, and A. M. Cremins-Costa, Time-resolved photoluminescence spectroscopy of Er-implanted porous silicon, J. Lumin. **71,** 13 (1997).

[38] A. M. Dibos, M. Raha, C. M. Phenicie, and J. D. Thompson, Atomic Source of Single Photons in the Telecom Band, Phys. Rev. Lett. **120,** 243601 (2018).

[39] T. Böttger, C. W. Thiel, Y. Sun, and R. L. Cone, Spectroscopy and dynamics of Er^{3+}: Y$_2$SiO$_5$ at 1.5 µm, Phys. Rev. B **74,** 075107 (2006).

[40] N. Q. Vinh, H. Przybylińska, Z. F. Krasil'nik, and T. Gregorkiewicz, Optical properties of a single type of optically active center in Si/Si:Er nanostructures, Phys. Rev. B **70,** 115332 (2004).

[41] A. Szabo, Observation of hole burning and cross relaxation effects in ruby, Phys. Rev. B **11,** 4512 (1975).

[42] G. C. Bjorklund, in *Persistent Spectral Hole-Burning: Science and Applications*, Vol. 1, edited by W. E. Moerner (Springer-Verlag Berlin Heidelberg, 1988), p. 5.

[43] Y. D. Huang, M. Mortier, and F. Auzel, Stark levels analysis for Er^{3+}-doped oxide glasses: Germanate and silicate, Opt. Mater. (Amst) **15,** 243 (2001).

[44] F. Priolo, G. Franzo, S. Coffa, A. Polman, S. Libertino, R. Barklie, and D. Carey, The erbium-impurity interaction and its effects on the 1.54 µm luminescence of Er^{3+} in crystalline silicon, J. Appl. Phys. **78,** 3874 (1995).

[45] N. Q. Vinh, S. Minissale, B. A. Andreev, and T. Gregorkiewicz, The Auger process of luminescence quenching in Si/Si:Er multinanolayers, J. Phys.: Condens. Matter **17,** S2191 (2005).

[46] See Supplemental Material at http://link.aps.org/supplemental/10.1103/PhysRevApplied.19.014037 for additional details on the lifetime measurements (S-B).

[47] C. M. Dodson and R. Zia, Magnetic dipole and electric quadrupole transitions in the trivalent lanthanide series: Calculated emission rates and oscillator strengths, Phys. Rev. B **86,** 125102 (2012).

[48] T. G. Brown and D. G. Hall, Optical-emission at 1.32 µm from sulfur-doped crystalline silicon, Appl. Phys. Lett. **49,** 245 (1986).

[49] F. Marsili, V. B. Verma, J. A. Stern, S. Harrington, A. E. Lita, T. Gerrits, I. Vayshenker, B. Baek, M. D. Shaw, R. P. Mirin, and S. W. Nam, Detecting single infrared photons with 93% system efficiency, Nat. Photonics **7,** 210 (2013).

[50] D. Istrati, Y. Pilnyak, J. C. Loredo, C. Anton, N. Somaschi, P. Hilaire, H. Ollivier, M. Esmann, L. Cohen, L. Vidro, C. Millet, A. Lemaitre, I. Sagnes, A. Harouri, L. Lanco, P. Senellart, and H. S. Eisenberg, Sequential generation of linear cluster states from a single photon emitter, Nat. Commun. **11,** 5501 (2020).

[51] T. Zhong, J. M. Kindem, J. G. Bartholomew, J. Rochman, I. Craiciu, V. Verma, S. W. Nam, F. Marsili, M. D. Shaw, A. D. Beyer, and A. Faraon, Optically Addressing Single Rare-Earth Ions in a Nanophotonic Cavity, Phys. Rev. Lett. **121,** 183603 (2018).

[52] M. Yamaguchi, T. Asano, M. Fujita, and S. Noda, Theoretical analysis of light emission from a coupled system of a photonic nanocavity and a quantum dot, Physica Status Solidi (C) **5,** 2828 (2008).

[53] J. Zhou, J. J. Zheng, Z. R. Fang, P. P. Xu, and A. Majumdar, Ultra-low mode volume on-substrate silicon nanobeam cavity, Opt. Express **27,** 30692 (2019).

[54] R. Miura, S. Imamura, R. Ohta, A. Ishii, X. Liu, T. Shimada, S. Iwamoto, Y. Arakawa, and Y. K. Kato, Ultralow mode-volume photonic crystal nanobeam cavities for high-efficiency coupling to individual carbon nanotube emitters, Nat. Commun. **5,** 5580 (2014).

[55] E. Kuramochi, H. Taniyama, T. Tanabe, K. Kawasaki, Y. G. Roh, and M. Notomi, Ultrahigh-Q one-dimensional photonic crystal nanocavities with modulated mode-gap barriers on SiO$_2$ claddings and on air claddings, Opt. Express **18,** 15859 (2010).

[56] S. Hu, M. Khater, R. Salas-Montiel, E. Kratschmer, S. Engelmann, W. M. J. Green, and S. M. Weiss, Experimental realization of deep-subwavelength confinement in dielectric optical resonators, Sci. Adv. **4,** eaat2355 (2018).

[57] A. Gritsch, L. Weiss, J. Früh, S. Rinner, and A. Reiserer, Narrow Optical Transitions in Erbium-Implanted Silicon Waveguides, Phys. Rev. X **12,** 041009 (2022).